MIT Libraries | DSpace@MIT

MIT Open Access Articles

Impact of Vegetation on Bed Load Transport Rate and Bedform Characteristics

The MIT Faculty has made this article openly available. ***Please share*** how this access benefits you. Your story matters.

Citation: Yang, J. Q. and H. M. Nepf, "Impact of Vegetation on Bed Load Transport Rate and Bedform Characteristics." Water Resources Research 55, 7 (July 2019): 6109-24 doi. 10.1029/2018WR024404 ©2019 Authors

As Published: https://dx.doi.org/10.1029/2018WR024404

Publisher: American Geophysical Union (AGU)

Persistent URL: https://hdl.handle.net/1721.1/125735

Version: Final published version: final published article, as it appeared in a journal, conference proceedings, or other formally published context

Terms of Use: Article is made available in accordance with the publisher's policy and may be subject to US copyright law. Please refer to the publisher's site for terms of use.

Massachusetts Institute of Technology

Water Resources Research

RESEARCH ARTICLE
10.1029/2018WR024404

Key Points:
- Turbulent kinetic energy and bed load transport rate were predicted from velocity and vegetation volume fraction
- Vegetation-generated turbulence impacts the bed load transport rate by controlling the number of grains in motion
- Vegetation of sufficient volume fraction suppressed bedform formation

Supporting Information:
- Supporting Information S1

Correspondence to:
J. Q. Yang,
qjyang@mit.edu

Citation:
Yang, Q. J., & Nepf, H. M. (2019). Impact of vegetation on bed load transport rate and bedform characteristics. *Water Resources Research*, *55*. https://doi.org/10.1029/2018WR024404

Received 10 NOV 2018
Accepted 25 JUN 2019
Accepted article online 4 JUL 2019

©2019. American Geophysical Union. All Rights Reserved.

Impact of Vegetation on Bed Load Transport Rate and Bedform Characteristics

J. Q. Yang[1] and H. M. Nepf[1]

[1]Department of Civil and Environmental Engineering, Massachusetts Institute of Technology, Cambridge, MA, USA

Abstract The impacts of aquatic vegetation on bed load transport rate and bedform characteristics were quantified using flume measurements with model emergent vegetation. First, a model for predicting the turbulent kinetic energy, k_t, in vegetated channels from channel average velocity U and vegetation volume fraction ϕ was validated for mobile sediment beds. Second, using data from several studies, the predicted k_t was shown to be a good predictor of bed load transport rate, Q_s, allowing Q_s to be predicted from U and ϕ for vegetated channels. The control of Q_s by k_t was explained by statistics of individual grain motion recorded by a camera, which showed that the number of sediment grains in motion per bed area was correlated with k_t. Third, ripples were observed and characterized in channels with and without model vegetation. For low vegetation solid volume fraction ($\phi \leq 0.012$), the ripple wavelength was constrained by stem spacing. However, at higher vegetation solid volume fraction ($\phi = 0.025$), distinct ripples were not observed, suggesting a transition to sheet flow, which is sediment transport over a plane bed without the formation of bedforms. The fraction of the bed load flux carried by migrating ripples decreased with increasing ϕ, again suggesting that vegetation facilitated the formation of sheet flow.

1. Introduction

Aquatic vegetation provides tens of trillion of dollars worth of ecosystem services annually (Costanza et al., 1997), such as reducing flood damage (Narayan et al., 2017) and removing contaminants in water (Jenkins et al., 2010). However, large areas of aquatic vegetation, including half of the world's wetlands (Zedler & Kercher, 2005), have been lost in the past several decades and continue to be lost globally at rates of 0.7% to 7% annually (McLeod et al., 2011). One reason for the loss of vegetated landscapes is erosion (Blum & Roberts, 2009; Fagherazzi et al., 2013). Understanding the impact of vegetation on bed load transport and bedform migration will improve our ability to predict erosion rates in regions with vegetation.

Current bed load transport models, based on the time-mean bed shear stress τ, were developed for unidirectional flow without obstacles, and these models have been shown to be inaccurate for regions with obstacles, such as bedforms and vegetation (e.g., Nelson et al., 1995; Yager & Schmeeckle, 2013). The inaccuracy of the τ-based bed load transport models in vegetated channels has been attributed to the following: (1) Bare-bed models for bed shear stress τ are inaccurate in vegetated channels and prone to large errors, and (2) τ is not the (main) driver of bed load transport, and the role of vegetation-generated turbulence must also be considered (e.g., Nepf, 2012a; Yang & Nepf, 2018). It is well recognized that turbulence plays an important role in bed load transport (e.g., Heathershaw & Thorne, 1985; Mazumder, 2000; Salim et al., 2017; Schmeeckle, 2014; Sumer & Oguz, 1978). Previous studies have described the impact of turbulent structures (e.g., Nelson et al., 1995), velocity fluctuations (e.g., Sumer et al., 2003), and the duration of the peak velocity (e.g., Diplas et al., 2008) on bed load transport. Recent studies demonstrated that, in regions with vegetation, sediment transport is more closely correlated with turbulent kinetic energy, k_t, than with the time-mean bed stress (τ) (Tinoco & Coco, 2016, 2018; Yang & Nepf, 2018; Yager & Schmeeckle, 2013; Yang et al., 2016). Specifically, within a channel of model vegetation, Yager and Schmeeckle (2013) observed that regions of high bed load transport are correlated with high near-bed turbulence. Yang et al. (2016) showed that k_t is a better predictor of the threshold of sediment motion than τ and that the critical level of near-bed turbulence is the same in bare and vegetated channels. Similarly, Tinoco and Coco (2016, 2018) showed that resuspension of sediment within an array of model vegetation is better predicted by a metric based on k_t than τ. Finally, Yang and Nepf (2018) demonstrated that the bed load transport rate, Q_s, was better correlated with k_t than τ, and they attributed the dependence of Q_s on k_t to the fact that the lift force on the sediment grains, which initiates

sediment transport (e.g., Nino & Garcia, 1996; Sumer & Oguz, 1978; Vollmer & Kleinhans, 2007; Zanke, 2003), scales with k_t (Batchelor, 1951; Dittrich, 1998; Zanke, 2003).

In response to bed load transport, bedforms are often generated (Southard, 1991; Van Rijn, 2007). The bedforms can migrate with flow and modify the flow structure (Best, 2005; Julien, 2010; Soulsby et al., 2012). This study considered ripples, which are small bedforms with wave heights less than a few centimeters (Julien, 2010). In regions without vegetation, the ripple height and the migration speed have been related to the water velocity U (Chang, 1939; Damgaard et al., 2003; Poos, 2011; Southard, 1991), and the ripple wavelength was shown to mainly depend on sediment size (Baas, 1993; Soulsby et al., 2012). The sediment transport associated with the migration of ripples has been shown to be a good approximation for total bed load transport in bare channels (Crickmore, 1970; Damgaard et al., 2003). In contrast with bare channel cases, the presence of vegetation has been observed to reduce and even suppress bedforms in rivers (Nepf, 2012b; Przyborowski et al., 2018). Understanding how vegetation affects bedforms is important because vegetation is ubiquitous in nature. However, there is still a lack of quantitative understanding of how vegetation with different volume fractions affects bedform characteristics and bedform migration rate.

The present study builds on the work of Yang and Nepf (2018), who showed that bed load transport, Q_s, is correlated with measured near-bed turbulence, k_t, in both bare and vegetated channels. In this paper, we extend this result in the following important ways. First, we show that k_t in vegetated channels with mobile beds can be predicted from velocity U and vegetation volume fraction ϕ. Second, by using the model for k_t, we show that the bed load transport can be predicted from just U and ϕ. Third, statistics of individual grain motion are used to understand the connection between turbulence and bed load transport. Finally, this paper quantifies the impact of vegetation on the bedform characteristics and migration rate.

2. Theory

2.1. Prediction of Turbulent Kinetic Energy in Vegetated Channels

Yang et al. (2016) extended the model proposed by Tanino and Nepf (2008) to describe the near-bed turbulent kinetic energy, k_t, as the sum of the bed-generated turbulence and vegetation-generated turbulence

$$k_t = \underbrace{\frac{\tau}{0.19\rho}}_{\text{bed-generated } (k_{t(\text{bed})})} + \underbrace{\delta_{k_t}\left[C_D\frac{\phi}{(1-\phi)\pi/2}\right]^{2/3}U^2}_{\text{vegetation-generated } (k_{t(\text{veg})})}. \tag{1}$$

Here the bed-generated turbulent kinetic energy, the first term on the right-hand side, is proportional to the bed shear stress τ divided by water density ρ (Hofland & Battjes, 2006; Stapleton & Huntley, 1995). The vegetation-generated turbulent kinetic energy is a function of a scaling constant δ_{k_t}, the vegetation drag coefficient C_D, the vegetation volume fraction ϕ, and pore velocity U. The pore velocity $U = Q/(wh(1-\phi))$ with Q, w, and h representing flow rate, channel width, and water depth, respectively. Yang et al. (2016) validated equation (1) for a fixed bed with glued grains. Here we consider whether equation (1) can be used to estimate k_t for a mobile sand bed. Note that this model assumes the vegetation has a rigid cylindrical morphology with diameter d, such that $\phi = n\pi d^2/4$, with n the number of stems per bed area. Some adjustment is needed to accommodate noncylindrical or flexible morphology (see Zhang et al., 2018).

In this study we consider a model vegetation consisting of rigid, circular cylinders in a square, staggered array. For this configuration, the drag coefficient C_D can be estimated from the following equation derived from Large Eddy Simulation (Etminan et al., 2017),

$$C_D = \zeta^2\left[1 + 10\left(\frac{\zeta U d}{\nu}\right)^{-2/3}\right]. \tag{2}$$

Here ν is the kinematic viscosity. The coefficient $\zeta = \frac{1-\phi}{1-\sqrt{2\phi/\pi}}$ represents the ratio of the average velocity at the point of maximum flow constriction, that is, in between adjacent cylinders, to the pore velocity, U.

The bed shear stress τ in both bare and vegetated channels can be estimated using the linear stress model proposed by Yang et al. (2015):

$$\tau = \frac{2\rho\nu U}{H_v}. \tag{3}$$

Here H_v is the thickness of the viscous layer. For bare channels, $H_v = \frac{2\nu}{C_f U}$, with C_f the bed drag coefficient, so that $\tau = \rho C_f U^2$. For channels with emergent cylindrical stems, we use the approximation $H_v = \min(\frac{d}{2}, \frac{2\nu}{C_f U})$ proposed in Yang et al. (2015) to estimate τ. At high stem Reynolds number $Re_d = Ud/\nu > 4/C_f$, the viscous layer thickness $H_v = \min(\frac{d}{2}, \frac{2\nu}{C_f U}) = \frac{2\nu}{C_f U}$ so that the impact of vegetation on bed shear stress is negligible and $\tau = \rho C_f U^2$. Note that $H_v = \min(\frac{d}{2}, \frac{2\nu}{C_f U})$ is a reasonable approximation when the stem Reynolds number $Re_d > 1,200$, which is true for all conditions considered here (based on Figure 14 in Etminan et al., 2018). For $Re_d < 600$ and vegetation volume fraction $\phi > 0.1$, an improved H_v approximation model has been proposed by Etminan et al. (2018). For turbulent flow, C_f can be estimated from the sediment size d_s and water depth h using the semiempirical equation (Whiting & Dietrich, 1990; Julien, 2010):

$$C_f = \frac{1}{[5.75\log(2h/d_s)]^2}. \tag{4}$$

2.2. Models for Bed Load Transport Rate

For bare channels, Einstein (1950) and Brown (1950) proposed the following bed shear stress model to predict bed load transport rate:

$$Q_{s*} = \begin{cases} 2.15e^{-0.391/\tau_*}, & \tau_* < 0.18 \\ 40\tau_*^3, & 0.18 < \tau_* < 0.52. \end{cases} \tag{5}$$

The dimensionless bed load transport rate, Q_{s*}, is defined as the ratio of the bed load transport rate Q_s to the product of sediment density, ρ_s, the fall velocity of the grains (ω_0), and the grain size (d_s),

$$Q_{s*} = \frac{Q_s}{\rho_s \omega_0 d_s}. \tag{6}$$

The particle fall velocity ω_0 can be approximated from the Rubey's (1933) equation

$$\omega_0 = \left[\sqrt{\frac{2}{3} + \frac{36\nu^2}{(\rho_s/\rho - 1)gd_s^3}} - \sqrt{\frac{36\nu^2}{(\rho_s/\rho - 1)gd_s^3}}\right]\sqrt{(\rho_s/\rho - 1)gd_s}. \tag{7}$$

The dimensionless bed shear stress, τ_*, represents the ratio of the horizontal force exerted on the grain, $\tau(\pi d_s^2/4)$, to the submerged weight of the grain, $(\rho_s - \rho)g(\pi d_s^3/6)$,

$$\tau_* = \frac{\tau}{(\rho_s - \rho)gd_s}. \tag{8}$$

In vegetated channels, Yang and Nepf (2018) showed that the bed load transport rate, Q_s, is a function of k_t instead of the bed shear stress, τ. They attributed the control of Q_s by k_t to the fact that bed load transport is initiated by a turbulence-induced lift force (Bagnold, 2012; Nino & Garcia, 1996; Smart & Habersack, 2007; Sumer & Oguz, 1978), which is proportional to the turbulent kinetic energy k_t (Dittrich, 1998; Zanke, 2003). Based on this, Yang and Nepf (2018) converted the τ-based Einstein-Brown model to a k_t-based model. Specifically, the Einstein-Brown equation is based on measurements in a bare channel, for which $k_t = \tau/0.19\rho$ (Hofland & Battjes, 2006; Stapleton & Huntley, 1995), from which Yang and Nepf (2018) suggested the following k_t-based bed load model:

$$Q_{s*} = \begin{cases} 2.15e^{-2.06/k_{t*}}, & k_{t*} < 0.95 \\ 0.27k_{t*}^3, & 0.95 < k_{t*} < 2.74. \end{cases} \tag{9}$$

Here the dimensionless turbulent kinetic energy

$$k_{t*} = \frac{k_t}{(\rho_s/\rho - 1)gd_s} \tag{10}$$

represents the ratio of the turbulence-induced lift force, which is proportional to $\rho k_t(\pi d_s^2/4)$ (Batchelor, 1951; Dittrich, 1998; Zanke, 2003), to the submerged weight of the grain, $(\rho_s - \rho)g(\pi d_s^3/6)$.

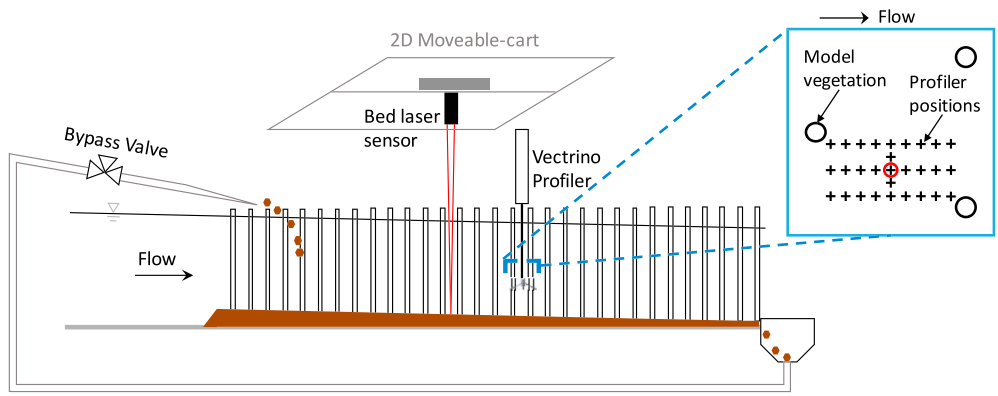

Figure 1. The sediment-recirculation experiment for measuring bed load transport rate and bedform characteristics. The brown color indicates the sand bed. The sand was recirculated separately from the water and returned to the flume slightly above the water surface along a 1-m-long tilted diffusor plate that distributed it uniformly across the width of the flume. At the beginning of each experiment, the sand bed was flat and level. After an experiment, the sand bed was sloped (as shown here), and ripples had formed (not shown). The blue-edged inset shows the top view of the velocity measurement positions (the crosses) relative to cylinder positions (the black circles). The vegetation volume fraction in the inset represents cases 3.1–3.3 ($\phi = 0.012$). To quantify ripple characteristics, bed elevation as a function of time was recorded by the Vectrino profiler at the position marked with a red circle.

3. Methods

Two sets of experiments were conducted in the same horizontal-bed channel, with a 1-m-wide and 10-m-long test section. The sediment-recirculating experiments studied bed load transport and bedform characteristics with a mobile sand bed. The sediment-tracking experiments quantified the statistics of individual grain motion. The model vegetation consisted of rigid cylinders with diameter $d = 6.3$ mm placed in a staggered pattern and extending above the water surface. This diameter was consistent with stem diameters found in marsh plants and young floodplain trees (Manners et al., 2015; Nepf, 2012a). When present, the model vegetation covered the entire flume width. The number of cylinders per unit bed area for the two sets of experiments presented here was in the range $n = 0$ to 1,550 stems per square meter, producing a vegetation frontal area per unit volume, $a = nd$, in the range 0 to 9.8 m^{-1} and a vegetation solid volume fraction $\phi = \pi n d^2/4 = 0$ to 0.05, which are typical values for marshes (Nepf, 2012a). The flow rate Q was controlled by a centrifugal pump and measured by a flow meter with 1 m^3/hr accuracy, the channel width $w = 1$ m, and the water depth h was measured using a ruler fixed at the flume wall in the streamwise center of the vegetation patch. The pore velocity in the vegetation test section was calculated as $U = Q/(wh(1-\phi))$.

3.1. Setup for the Sediment-Recirculation Experiment

In the sediment-recirculation experiment, water and sand were recirculated separately (Figure 1). The range of flow rates and vegetation solid volume fractions (ϕ) are given in Table 1. For cases 2.1–2.4 and 3.1–3.3, the vegetation covered 3 m in the streamwise direction. For cases 4.1–4.4, the densest cases considered for mobile beds, the vegetation covered only 2 m in the streamwise direction to minimize the impact of the large surface slope set up by the high vegetation drag and thus large variation in flow depth (>30%).

Before the start of each experiment, a 4-cm-thick layer of sand with density $\rho_s = 2.65$ g/cm^3 and diameter 0.42 to 0.60 mm (median grain size $d_s = 0.5$ mm) was placed on the bed and flattened manually. Once the flow was initiated, sediment moving along the channel was captured in a sediment trap at the end of the channel and recirculated back to the upstream end of the test section through a separate line (Figure 1). No sand was observed in suspension during the experiment. The bed load transport rate, defined as the dry mass of the sediment passing an unit cross-sectional width per time, was measured by collecting the recirculating sediment through a bypass valve in the sediment return pipe and measuring its dry weight. More details about this measurement are presented in Supporting Information S1. Multiple bed load transport rates were measured, and the flow was assumed to reach equilibrium once the cumulative average of all bed load measurements varied by less than 10%, which took 6 to 40 hr depending on the flow condition. We note that in previous studies of very low bed load transport rate (less than 10 grains per (m · s)), temporal fluctuations were observed over much longer time scales, such that the time needed to reach equilibrium may be much larger than 40 hr (Ancey et al., 2015; Dhont & Ancey, 2018). The equilibrium bed load transport rate and its

Table 1
The Measured Bed Load Transport Rate and Flow Characteristics

Case number	a (m^{-1})	ϕ	U (m/s)	h (m)	$Q_s \pm \sigma_{Q_s}$ (g/(m · s))	$k_t \pm \sigma_{k_t}$ (cm^2/s^2)
Bare channels						
1.1	0	0	0.42	0.12	0.36 ± 0.05 (28)	28 ± 1 (8)
1.2	0	0	0.47	0.12	1.84 ± 0.08 (10)	46 ± 1 (34)
1.3	0	0	0.65	0.12	24 ± 1 (6)	111 ± 11 (8)
1.4	0	0	0.88	0.12	134 ± 8 (9)	205 ± 10 (8)
Channels with emergent vegetation						
2.1	1.1	0.005	0.27	0.12	0.5 ± 0.1 (32)	19 ± 3 (24)
2.2	1.1	0.005	0.30	0.12	2.5 ± 0.3 (21)	20 ± 2 (24)
2.3	1.1	0.005	0.34	0.12	9 ± 1 (12)	32 ± 5 (24)
2.4	1.1	0.005	0.43	0.12	68 ± 17 (10)	65 ± 8 (24)
3.1	2.5	0.012	0.21	0.12	0.15 ± 0.02 (32)	17 ± 2 (27)
3.2	2.5	0.012	0.24	0.12	2.6 ± 0.5 (9)	22 ± 2 (27)
3.3	2.5	0.012	0.28	0.12	9.4 ± 0.6 (15)	45 ± 5 (27)
4.1	5.1	0.025	0.21	0.10	1.3 ± 0.1 (22)	20 ± 2 (23)
4.2	5.1	0.025	0.23	0.10	2.9 ± 0.3 (36)	42 ± 4 (23)
4.3	5.1	0.025	0.27	0.10	17 ± 1 (25)	46 ± 4 (23)
4.4	5.1	0.025	0.31	0.10	41 ± 2 (21)	51 ± 5 (23)

Note. The number in parentheses next to $Q_s \pm \sigma_{Q_s}$ represents the experimental duration in hours, which is the time from the beginning of the experiment to when the last bed load transport measurement was made. The number in parentheses next to $k_t \pm \sigma_{k_t}$ indicates the number of spatial positions at which velocity measurements were made.

uncertainty, $Q_s \pm \sigma_{Q_s}$, were calculated as the average and standard error of all bed load measurements and are listed in Table 1.

The instantaneous velocity in the streamwise, spanwise, and vertical direction (u, v, and w, respectively) was measured by a Nortek Vectrino profiler at 100-Hz sampling rate for 3 min at multiple locations in the middle of the vegetation patch (shown with crosses in the inset of Figure 1). The local turbulent kinetic energy was defined as $(\overline{u'^2} + \overline{v'^2} + \overline{w'^2})/2$, with u', v', and w' denoting the instantaneous deviation from the time-mean velocity and $(\overline{})$ denoting the time average. The spatially averaged turbulent kinetic energy and its uncertainty, $k_t \pm \sigma_{k_t}$, were calculated as the average and standard error of the local measurements. The estimate of near-bed turbulence level was made at 2 cm above the mean bed elevation to avoid high measurement noise near the mobile bed (see details in Yang & Nepf, 2018). For vegetated channels, k_t increases with increasing distance from the bed within a thin viscous layer and is vertically uniform above the viscous layer, so that measurements at 2 cm are representative of the maximum turbulent kinetic energy (Yang & Nepf, 2018). For bare channels, k_t has a narrow peak close to the bed so that the k_t measured at 2 cm can be up to 30% less than the maximum turbulent kinetic energy (Yang & Nepf, 2018). The measured $k_t \pm \sigma_{k_t}$ and the number of velocity measurements included in the spatial average are tabulated in Table 1.

Bedforms with heights up to 2 cm were observed during the experiment, and we classified them as ripples. To quantify the ripple height and migration period, the instantaneous bed elevation was recorded at 1-Hz sampling rate by a Vectrino profiler located at the middle of the diagonal between two dowels (the red circle in the inset of Figure 1). The duration of the measurement, ranging from 30 min to 2 hr, was chosen to be much longer than the ripple migration period (Table 2). The ripple crest to trough distance was identified using MATLAB findpeaks function (Figure 2a). The average and the standard deviation of all the identified crest-trough heights, $\eta_1 \pm SD(\eta_1)$, are listed in Table 2. The uncertainty in η_1 was estimated as the standard error of the crest-trough heights, that is, $\sigma_{\eta_1} = SD(\eta_1)/\sqrt{m_1}$, with m_1 denoting the number of identified crest-trough heights (Table 2). The ripple migration period (T) was determined from time lag corresponding to the first positive peak at lag greater than zero in the autocorrelation of the bed elevation (Figure 2b). The

Table 2
The Measured Ripple Characteristics

Case number	ϕ	U (m/s)	$\lambda \pm \sigma_\lambda$ (m)	$\eta_1 \pm SD(\eta_1)$ (mm; # of ripples)	$\eta_2 \pm SD(\eta_2)$ (mm; # of ripples)	$T \pm \sigma_T$ (s)
Bare channels						
1.1	0	0.42	0.25 ± 0.03	6 ± 1 (5)	2 ± 1 (4)	880 ± 160
1.2	0	0.47	0.28 ± 0.05	11 ± 2 (9)	8 ± 1 (2)	660 ± 200
1.3	0	0.65	NA	11 ± 4 (16)	NA	38 ± 4
1.4	0	0.88	0.29 ± 0.09	13 ± 2 (7)	6 ± 5 (6)	40 ± 20
Channels with model emergent vegetation						
2.1	0.005	0.27	0.21 ± 0.06	3 ± 1 (3)	3 ± 1 (6)	$2,400 \pm 300$
2.2	0.005	0.30	0.16 ± 0.04	3 ± 1 (8)	3 ± 1 (7)	630 ± 160
2.3	0.005	0.34	0.17 ± 0.04	7 ± 3 (17)	7 ± 3 (4)	110 ± 50
2.4	0.005	0.43	0.17 ± 0.03	12 ± 5 (52)	10 ± 3 (6)	42 ± 11
3.1	0.012	0.21	0.10 ± 0.02	2 ± 1 (4)	3 ± 1 (8)	$4,600 \pm 800$
3.2	0.012	0.24	0.10 ± 0.02	4 ± 1 (2)	6 ± 2 (8)	$2,300 \pm 500$
3.3	0.012	0.28	0.16 ± 0.06	6 ± 2 (52)	6 ± 3 (5)	200 ± 110
4.1	0.025	0.21	NA	2 ± 1 (12)	NA	$1,800 \pm 300$
4.2	0.025	0.23	NA	2 ± 1 (7)	NA	$1,500 \pm 500$
4.3	0.025	0.27	NA	3 ± 1 (47)	NA	29 ± 12
4.4	0.025	0.31	NA	2 ± 1 (55)	NA	30 ± 20

Note. λ and η_2, measured by the laser sensor, were not reported for case 1.3, because the laser measurement was contaminated by the reflection of the laser signal from the water surface. "NA" in the table means no measurement was taken for this case.

uncertainty in T, denoted as σ_T, was estimated as half the range of the first positive lobe (the positive lobe is indicated by the black color part of the curves in Figure 2b).

At the end of each experiment, the bed topography was scanned using a Keyence laser sensor mounted on a 2-D moving system (Figure 1). Two bed elevation profiles are shown in Figure 3a. The two profiles were measured 5 cm apart laterally and covered 50 cm in the streamwise direction. The streamwise center of the profiles was located at the streamwise center of the vegetation patch. The ripple profiles (Figure 3b) were

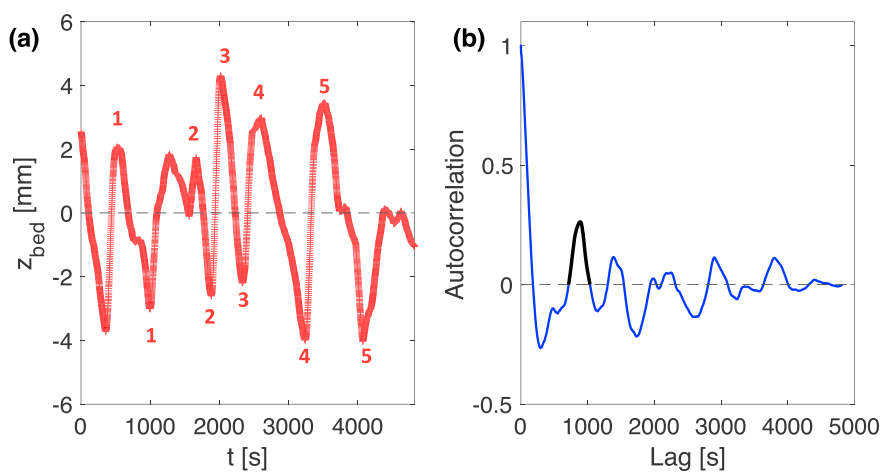

Figure 2. (a) The instantaneous bed elevation relative to the mean, z_{bed}, for case 1.1 measured using the Vectrino for 80 min. The number of identified ripples is 5 for this case, as listed in Table 2 and numbered in the figure. Only complete ripples were included in the counting, and variations in bed elevation that do not pass through the mean bed elevation were excluded from the counting. (b) The autocorrelation of bed elevation. The ripple migration period and its uncertainty, $T \pm \sigma_T = 880 \pm 160$ s, were identified from the time lag corresponding to the first positive peak at lag greater than zero (highlighted by a black curve above).

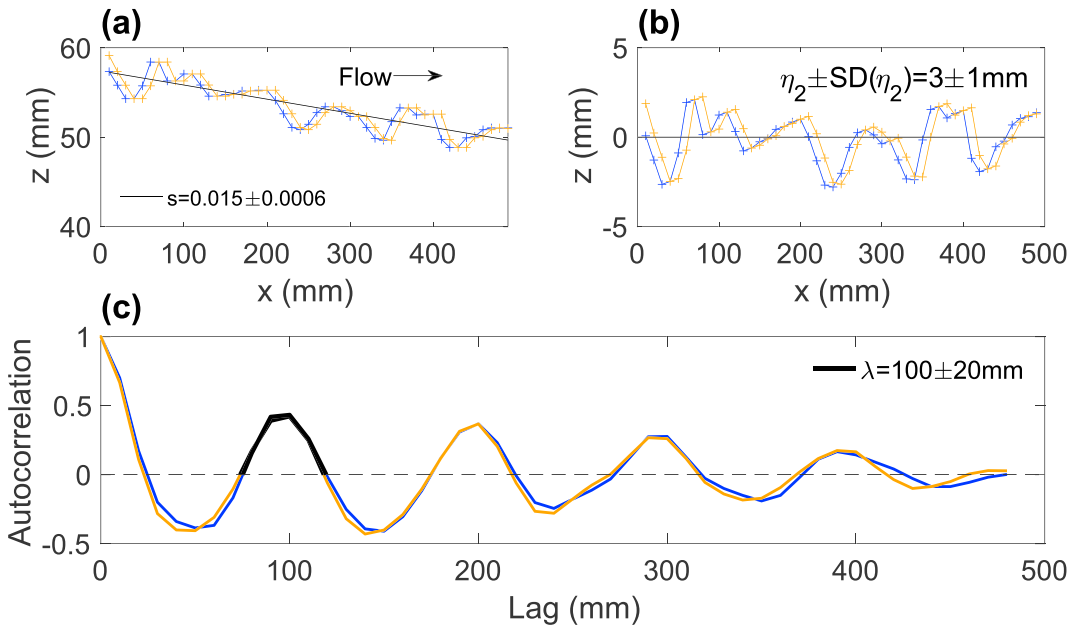

Figure 3. (a) Two bed topography profiles, indicated with different colors, measured 5 cm apart for case 3.1. Note that the x and z axes are plotted in different scales. (b) The detrended profiles obtained by subtracting the fitted mean bed slope (the black line in (a)) from the bed topography profiles. (c) The spatial autocorrelation of the ripple profiles with x axis representing the lag in distance. The first autocorrelation peak at lag greater than zero, indicated by black overlay curve, was used to estimate the ripple wavelength λ. The uncertainty σ_λ was half the range of the positive lobe.

obtained by subtracting the bed slope (the fitted black line in Figure 3a) from the bed elevation profiles. The ripple crest to trough distance was identified using MATLAB findpeaks function, and the number of identified ripples is listed in Table 2. The ripple height and its spatial variation, $\eta_2 \pm SD(\eta_2)$, were estimated as the average and the standard deviation of the identified crest-trough distances (Table 2). The ripple wavelength, λ, was determined from the distance lag corresponding to the first positive peak with greater than zero lag in the spatial autocorrelation of the bed elevation (Figure 3c). The uncertainty of the ripple wavelength, σ_λ, was half the range associated with the positive part of the chosen peak, shown with black curve. For cases 4.1–4.4 with the densest vegetation, the laser signal experienced too much interference from the closely spaced dowels, so η_2 and λ could not be determined. During the experiments, no part of the flume bed was exposed, and the maximum ripple amplitude (1 cm) was less than the sediment layer depth (4 cm). Based on these observations, we assumed that the availability of sediment was not limiting the formation of ripples. The small size of the ripples also limited their impact on near-bed turbulence and bed stress. Specifically, the lee-side angle of the ripples in our study was less than 20°. Previous high-resolution Laser Doppler Velocimeter measurements over bedforms with different shapes (Kwoll et al., 2016) have shown that for low-angle bedforms, defined as having slopes less than 20°, the bedform-induced flow separation was absent, and the bedforms increased the bed shear stress τ by less than 33% compared with flat beds (Kwoll et al., 2016). Because the lee-side angle of the ripples in our study was less than 20°, the impact of ripples on near-bed turbulence and bed shear stress were assumed to be negligible. The impact of migrating ripples on the spatially averaged turbulent kinetic energy k_t is discussed in more detail in Supporting Information S1.

3.2. The Sediment-Tracking Experiment

In addition to measuring the channel-scale bed load transport rate Q_s, as described in section 3.1, the statistics of individual grain motion were also considered. This gave a different perspective on how turbulence impacts bed load transport. Specifically, bed load transport can also be estimated from U_p, the average velocity of the grains in motion, and γ, the volume of moving grains per unit bed area, that is, $Q_s = U_p\gamma$ (Ancey et al., 2008; Furbish et al., 2012; Wong et al., 2007). Experiments tracking individual grain motion were used to estimate U_p and γ. One layer of sieved light-brown sand with diameter 0.60 to 0.85 mm was glued to the top of the baseboards. One layer of mobile black sand with the same size distribution was sprayed on top of the glued brown sand. The motion of the black sand was recorded using a digital camera at 60 frames per second for 30 s, and the trajectories of each black grain was identified using the particle tracking MatLab

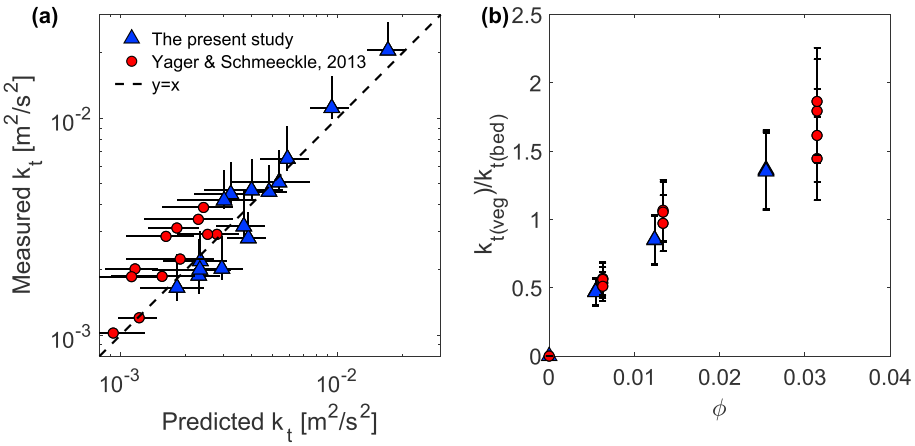

Figure 4. (a) The measured turbulent kinetic energy (k_t) versus the turbulent kinetic energy described by equations (1)–(4) and (b) the ratio of the vegetation-generated turbulence to the bed-generated turbulence, $k_{t(\mathrm{veg})}/k_{t(\mathrm{bed})}$, based on equations (1)–(4). The scaling constant $\delta_{k_t} = 0.4 \pm 0.3$ in equation (1) was obtained by least square fitting of equation (1) to the measurements. The triangles and circles are measurements from the present study and Yager and Schmeeckle (2013), respectively. The vertical error bars in (a) represent the spatial variation in the measured k_t and also incorporate the additional possible 30% underprediction of bed-generated turbulence for the present data, as discussed in section 3. The horizontal error bars in (a) represent the uncertainty in the predicted k_t propagated from the uncertainty in the scaling factor ($\delta_{k_t} = 0.4 \pm 0.3$) as well as the uncertainties in C_f and C_D, which were estimated as 20% and 10% based on velocity measurements in Yang et al. (2016) and Large Eddy Simulation results in Etminan et al. (2017), respectively. The dashed line represents 1:1 agreement. The vertical error bars in (b) represent the uncertainty in $k_{t(\mathrm{veg})}/k_{t(\mathrm{bed})}$ due to uncertainties in C_f and C_D.

code written by Crocker and Grier (1996). For each frame, the percentage of pixels occupied by black sand grains was calculated. The area fraction of black sand occupancy averaged over 30 s was denoted as P_{blk}. In this study, P_{blk} varied between 2% and 10%. The streamwise velocity of individual black sand grains was calculated from the identified trajectories, and the average of all trajectories identified over 30 s was used to define the average particle velocity, U_p. An example image with superimposed trajectories is shown in Supporting Information S1. The black sand grains only occupied a fraction of the bed area. To estimate the total volume of sediment grains in motion per unit bed area, γ, we made the following two assumptions. First, in a fully mobile bed, sediment transport only occurs in the top layer (Houssais et al., 2015). Second, all grains have equal probability to be moved. With these assumptions, γ can be calculated from N_{blk}, the number of moving black particles observed over the 1,800 frames (30 s), the average volume of one sand grain ($V_{\mathrm{sand}} = \frac{1}{6}\pi d_s^3$ with $d_s = 0.73$ mm), and the percentage of the area occupied by the black sand, P_{blk}, also averaged over 1,800 frames. Specifically, $\gamma = N_{\mathrm{blk}} V_{\mathrm{sand}}/P_{\mathrm{blk}}$. In this study the particle activity converged to a stable value within 30 s, so that 30 s was deemed long enough to define the average. However, previous studies have noted variation in particle activity over time scales of several minutes to hours (Ancey et al., 2008), but variation over these longer time scales were not considered in this study.

4. Results

4.1. The Turbulent Kinetic Energy in Vegetated Channels

The measured turbulent kinetic energy, k_t, is plotted against the predicted k_t in Figure 4a, alongside data sets from Yager and Schmeeckle (2013). The prediction of k_t is based on equations (1)–(4), using only the pore velocity (U), the water depth (h), the grain size (d_s), and the model vegetation stem diameter (d) and solid volume fraction (ϕ). The scaling constant $\delta_{k_t} = 0.4$ (with ± 0.3 the 95% confidence interval) in equation (1) was obtained by least square fitting equation (1) to the measurements. For randomly distributed emergent cylinder arrays, Tanino and Nepf (2008) found $\delta_{k_t} = 1.2$. Note that Tanino and Nepf (2008) defined a form-drag coefficient, $C_{D_{\mathrm{form}}}$, whereas here, for convenience, we have used the full drag coefficient, C_D. Because the full drag contains both form and viscous components, $C_D \geq C_{D_{\mathrm{form}}}$, with the difference absorbed into the scale coefficient, δ_{k_t}. Based on this, we expect a lower value of δ_{k_t} for our study. Consistent with this, King et al. (2012) suggest $\delta_{k_t} = 0.8$ based on the calibration of a numerical simulation model of flow through real and model vegetation. The good agreement between the measured k_t and k_t predicted using the fitted scaling constant $\delta_{k_t} = 0.4 \pm 0.3$, with coefficient of determination $R^2 = 0.88$, supported the validity of equation (1) in

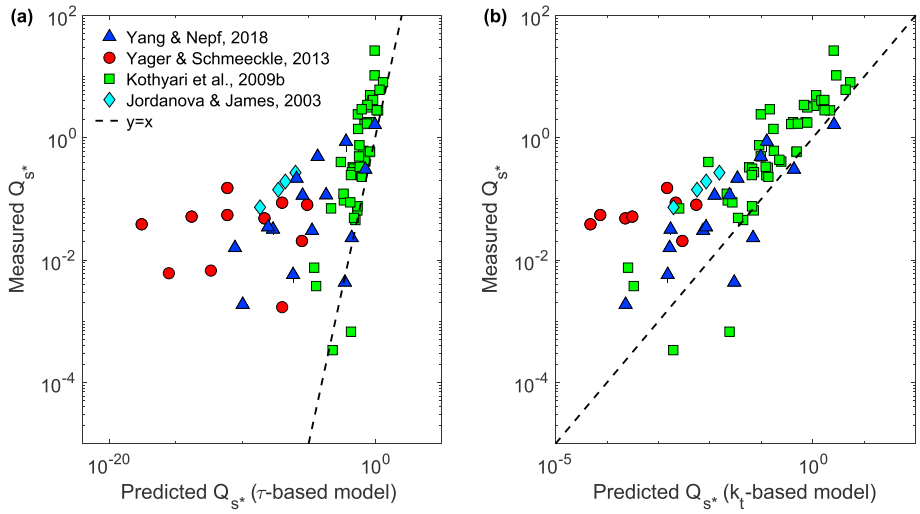

Figure 5. The measured dimensionless bed load transport rate Q_{s*} versus (a) Q_{s*} predicted by the τ-based model (equation (5)) and (b) the Q_{s*} predicted from U and ϕ using a combination of equations (1) and (9). The vertical error bars of the triangle symbols represent the uncertainty in the measured bed load transport rate. The dashed lines represent 1:1 agreement. Note that the x axis of (a) spanned over 20 orders of magnitude.

predicting the near-bed turbulent kinetic energy in vegetated channels with mobile beds. Note that for Yager and Schmeeckle (2013), the measured k_t was calculated as $k_t = (2\overline{u'^2} + \overline{w'^2})/2$ assuming $\overline{u'^2} \approx \overline{v'^2}$, because only streamwise velocity (u) and vertical velocity (w) were measured in Yager and Schmeeckle (2013). The approximation, $\overline{u'^2} \approx \overline{v'^2}$, was justified by previous velocity measurements (Tanino & Nepf, 2007).

The ratio of the vegetation-generated turbulent kinetic energy ($k_{t(\mathrm{veg})}$) to the bed-generated turbulent kinetic energy ($k_{t(\mathrm{bed})}$), as defined in equation (1), is shown in Figure 4b. For both the present data and data from Yager and Schmeeckle (2013), $k_{t(\mathrm{bed})}$ is larger than $k_{t(\mathrm{veg})}$ for $\phi \leq 0.01$, and for $\phi > 0.01$, the vegetation-generated turbulence starts to dominate. Recall that, in the present study, the impact of migrating ripples on k_t was negligible (Figure S2), because the ripple height was small ($\leq$1 cm) and the lee-side angles of the ripples were less than 20°. However, bedforms with larger size (height and/or lee-side angle) can generate additional turbulence, which would require a modification to the k_t relationship (equation (1)) and affect sediment transport (Bennett & Best, 1995; Best, 2005; Ma et al., 2017).

4.2. The Bed Load Transport Rate in Vegetated Channels

We next consider whether equations (1) and (9) could be combined to predict bed load transport from the pore velocity and vegetation solid volume fraction, that is, by first predicting the near-bed k_t from equation (1) and then using the predicted k_t in equation (9). In addition, we compared the prediction of bed load transport based on a classic bed stress model to the prediction by the k_t-based model using data sets from several studies. The measured dimensionless bed load transport rate Q_{s*} (equation (6)) was plotted against the Q_{s*} predicted using the τ-based model (equation (5)) and the Q_{s*} predicted using a combination of equations (1) and (9) in Figures 5a and 5b, respectively. The triangles are measurements from the present study. The circles represent measurements from Yager and Schmeeckle (2013) in which Q_{s*} was inferred from digital image analysis of the bed. The squares and the diamonds represent bed load transport rate measurements in vegetated channels estimated from the mass of the sediment leaving a flume (Kothyari et al., 2009) and the mass of sediment fed into a sediment-feed flume (Jordanova & James, 2003), respectively. In spite of the differences in the methods used to measure Q_{s*}, the agreement between the measured Q_{s*} and the Q_{s*} predicted using the k_t-based model, or equations (1) and (9), was significantly better than the agreement with the Q_{s*} predicted by the τ-based model (equation (5)). Note that of all the studies, Kothyari et al. (2009) had the lowest range of vegetation volume fraction, $\phi \leq 0.012$, which may explain why their data has relatively good agreement with the τ-based model. Specifically, for these low values of solid volume fraction, the bed was the main contributor to the turbulence (Figure 4b), so that near-bed turbulence was strongly correlated with bed shear stress. To quantitatively compare the two predictions, we estimated the root-mean-square deviation, defined as $RMSD = \sqrt{\sum_{j=1}^{m} (log(\hat{Q}_{s*}) - log(Q_{s*}))^2/m}$, with m, $\hat{Q}_{s*}$, and Q_{s*} representing the total number of measurements, the predicted dimensionless bed load transport rate, and the

measured dimensionless bed load transport rate, respectively. For the k_t-based model, equations (1) and (9), $RMSD = 0.9$, which was much smaller than $RMSD = 3.9$ for the τ-based model, confirming that k_t-model was better for predicting bed load transport and demonstrating that Q_s can be predicted from velocity U and vegetation volume fraction ϕ. We caution that for most of the cases, the measured Q_s was slightly higher than the Q_s predicted using the k_t-based model. However, this bias was much smaller than the impact of the vegetation-generated turbulence on Q_s. Consistently, our results (Figure 5) showed that the k_t-based method (equations (1) and (9)) was able to predict Q_s within 1 order of accuracy in vegetated channels, while the τ-based model underestimated Q_s by several orders of magnitude.

It is important to remember that k_t was measured 2 cm from the bed, which was above the laminar sublayer at the bed. In all cases considered here, the laminar sublayer was less than 3 mm. The individual grains ($d_s < 1$ mm) sit inside the laminar sub-layer. However, the turbulence above the laminar sublayer controls the pressure fluctuations and thus lift forces acting on the grains. Even though the eddies cannot penetrate into the boundary layer, the vertical pressure gradient induced by the turbulence outside the boundary layer can be transmitted to the boundary and affect sediment motion. This is consistent with the observation that the pressure signal in the outer boundary layer can trigger the turbulent bursting events in the inner boundary layer (Aubry et al., 1988). Note that the direction, duration, and sequence of turbulent events could also affect bed load transport (e.g., Diplas et al., 2008; Nelson et al., 1995; Shih et al., 2017). Therefore, more studies should be conducted to extend the k_t-based method developed for the vegetated channels to other situations.

4.3. The Velocity and Number of Moving Grains

Statistics of individual grain movement were used to explore how vegetation-generated turbulence affected the average velocity of the grains in motion, U_p, and the volume of moving grains per unit bed area, γ, which together provide another estimate of bed load transport $Q_s = U_p\gamma$ (Ancey et al., 2008; Furbish et al., 2012; Wong et al., 2007). Sediment motion can be initiated by turbulence-induced lift forces (e.g., Nino & Garcia, 1996; Sumer & Oguz, 1978; Vollmer & Kleinhans, 2007; Zanke, 2003), which scale with k_t (Batchelor, 1951; Dittrich, 1998; Zanke, 2003). Based on this, we hypothesize that the vegetation-generated turbulence may affect bed load transport by controlling γ. Previous sediment-tracking experiments in bare channels have noted that U_p increases linearly with the velocity U (e.g., Lajeunesse et al., 2010; Roseberry et al., 2012). Here we consider the dependence of U_p on both U and k_t in vegetated channels.

The mean grain velocity, U_p, normalized by the pore velocity, U, is shown for different solid volume fractions (ϕ) in Figure 6a. The pore velocity ranges from roughly 10 to 30 cm/s. For bare channels ($\phi = 0$), U_p/U is roughly a constant with $U_p/U \approx 0.21 \pm 0.01$, consistent with previous studies suggesting that U_p is proportional to U (e.g., Lajeunesse et al., 2010; Roseberry et al., 2012). For vegetated channels, U_p/U roughly increased with increasing solid volume fraction, and specifically, U_p/U at $\phi = 0.049$ was almost 50% larger than at $\phi = 0.005$, indicating that in vegetated channels, U_p was not a simple linear function of U and suggesting that U_p may also be a function of k_t, which also increased with increasing ϕ. The greater turbulence levels likely lifted individual particles farther from the bed, and, as noted in Nino and Garcia (1996), particles lifted higher above the bed achieve higher streamwise velocity. As the lift force scales with k_t (Batchelor, 1951; Dittrich, 1998; Zanke, 2003), the vertical acceleration of the particle and thus the distance the particle is lifted up from the bed, z_p, should also scale with k_t. Close to the bed, the streamwise velocity increases linearly with increasing distance from the bed, and the rate of increase is proportional to the pore velocity U. The lifted particle is accelerated by the streamwise velocity to which it is exposed, such that the particle's streamwise velocity, U_p, should depend on both U and $z_p \sim k_t$. To provide a dimensionally consistent parameter, U_p was assumed to scale with a linear combination of U and $\sqrt{k_t}$, namely, $U + \alpha\sqrt{k_t}$.

The value $\alpha = 10$ resulted in the smallest variation in $U_p/(U + \alpha\sqrt{k_t})$ across all ϕ, with the corresponding average and standard deviation of $U_p/(U + 10\sqrt{k_t}) = 0.09 \pm 0.01$, with no dependence of $U_p/(U + 10k_t)$ on ϕ (Figure 6b). This suggested that the impact of vegetation volume fraction on U_p was captured by the magnitude of k_t.

The dependence of γ on U and k_t are shown in Figures 6c and 6d. At the same pore velocity U, γ increased significantly with increasing ϕ (Figure 6c). In particular, at $U = 0.22$ m/s, γ increased by over 2 orders of magnitude as ϕ increased from 0 to 0.012, suggesting that the turbulence generated by the model vegetation significantly increased the number of sediment grains in motion. To test the hypothesis that k_t has a more important control on γ than U, γ was plotted against $k_t^{1/2}$ (m/s) in Figure 6d. Note that $k_t^{1/2}$ was used because

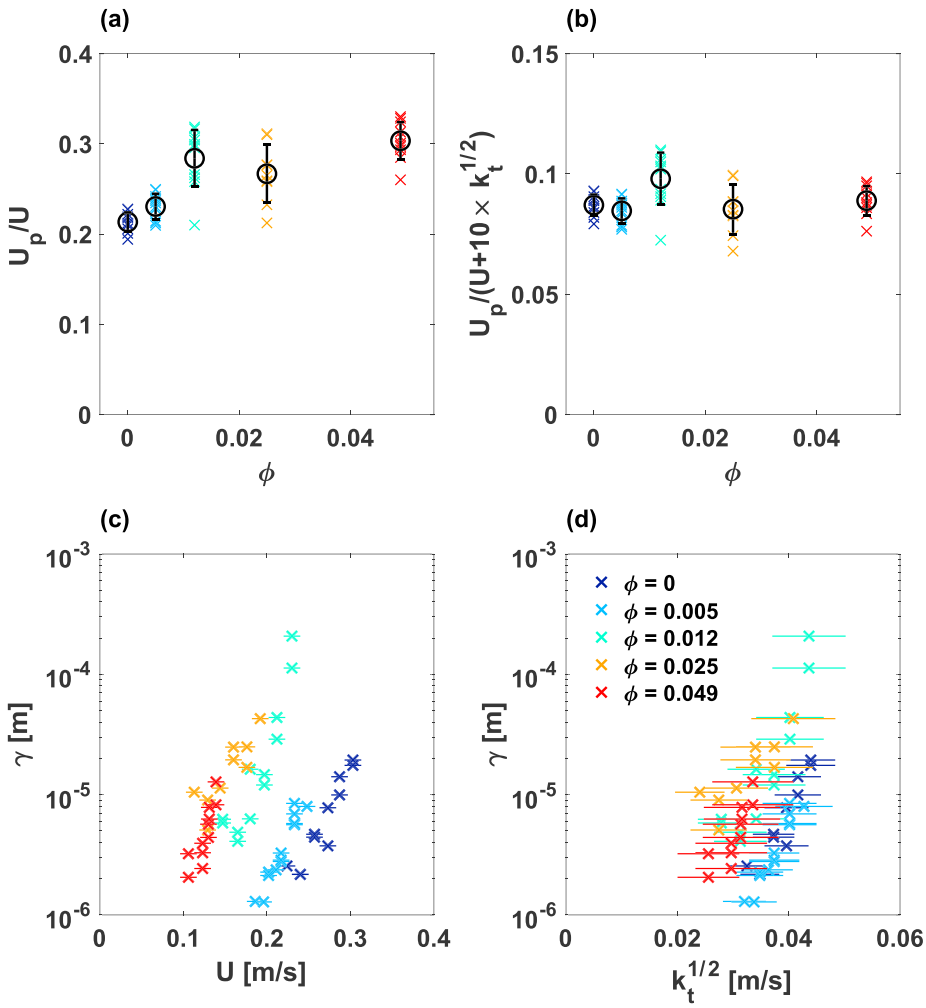

Figure 6. The colored crosses indicate individual measurements of (a) the mean particle velocity normalized by pore velocity, U_p/U, and (b) U_p normalized by the linear combination of U and $\sqrt{k_t}$ measured at different channel velocities (U) for each vegetation solid volume fraction ϕ. The black circles with error bars in (a) and (b) represent the average and the standard deviation over all the cases with different U for each ϕ. (c, d) The volume of particles in motion per bed area, γ, versus U and $\sqrt{k_t}$. The horizontal error bars in (c) represent the uncertainty in U due to fluctuations in flow rate, which is less than 10 m^3/hr. The horizontal error bars in (d) represent the uncertainty in $\sqrt{k_t}$ propagated from uncertainties in δ_{k_t} (±75%), C_f (±20%), and C_D (±10%). The legend in (d) applies to all figures.

it has the same unit (m/s) as U so that direct comparison can be made. At the same $k_t^{1/2}$, γ for different ϕ collapsed to within less than one order of magnitude, and no dependence of γ on ϕ was observed. The coefficient of determination, R^2, between $log(\gamma)$ and $\sqrt{k_t}$ was 0.23, much larger than the R^2 between $log(\gamma)$ and U ($R^2 = 0.02$), supporting our hypothesis that k_t is a better predictor of γ than U. Note that Roseberry et al. (2012) and Radice et al. (2009) also observed that γ fluctuates in space and time in response to the near-bed turbulent structures, further supporting the hypothesis that k_t is a better metric to predict the number of grains in motion than U. We caution that even though k_t was a better predictor of γ than U, the coefficient of determination between $log(\gamma)$ and $\sqrt{k_t}$ was still low ($R^2 = 0.23$), suggesting that other factors including U may also be important.

Because U_p is a function of both U and k_t (Figure 6b), the bed load transport rate ($Q_s = U_p\gamma$) would also be expected to be a function of both U and k_t. However, studies have shown that Q_s is predominantly controlled by the number of particles put in motion or γ (e.g., Radice & Ballio, 2008; Roseberry et al., 2012). Specifically, Radice and Ballio (2008) noted that with varying water velocity, the variation in γ is more significant than the variation in the sediment velocity, U_p. For a 40% increase in velocity, Roseberry et al. (2012) observed that γ increased by an over 2 orders of magnitude, but U_p increased by just a 60%. Considering all

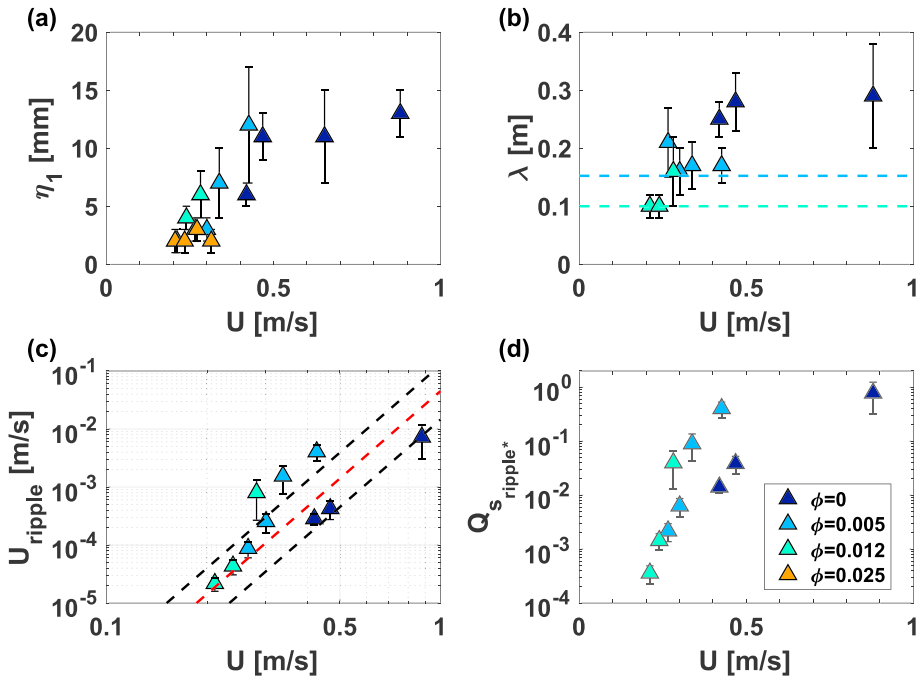

Figure 7. The ripple characteristics. (a) The ripple height (η_1) measured by the Vectrino and (b) the ripple wavelength (λ) measured by the laser sensor. For the cases with the densest vegetation ($\phi = 0.025$), the laser scanner was not reliable due to the interference from the closely spaced dowels such that λ was not estimated. In (b), the dashed horizontal lines indicate the mean spacing between neighboring dowels aligned in the streamwise direction. (c) The ripple migration speed $U_{\text{ripple}} = \lambda/T$. The red and black dashed lines represent the empirical relationship proposed by Chang (1939) for $d_s = 0.40$ mm: $U_{\text{ripple}}/U^5 = (4.5 \pm 0.6) \times 10^2$ (m/s)$^{-4}$. Note that the x axis was plotted in logarithmic scale to facilitate comparison of the present measurements with the Chang (1939) model. (d) The ripple migration rate estimated from equation (13) was normalized by $\rho_s \omega_0 d_s$. The legend in (d) applies to all figures.

the variations in U and ϕ in Figure 6, the measured U_p varied by less than a factor of 3 (from 2.4 to 7.1 cm/s), but γ varied by two orders of magnitude, from 3.0×10^{-8} to 4.3×10^{-6} m (Figure 6c), suggesting that the variation in Q_s was dominated by the variation in γ rather than U_p, which was consistent with both Radice and Ballio (2008) and Roseberry et al. (2012).

Because Q_s was mainly controlled by γ, which was better predicted by k_t, it is now clear why Q_s ($= U_p\gamma$) can be predicted by the k_t-based bed load model (equation (9)), as shown in Figure 5. However, we caution that in the experiments described in Figure 6, U varied by less than a factor of 3 ($U = 0.11$ to 0.30 m/s), which may not have been enough range to reveal a weaker dependence of Q_s on U. For all the flow conditions in all the experiments compiled in this study ($U = 0.11$ to 0.95 m/s and $\phi = 0$ to 0.049), the k_t-based model provided a reasonable prediction for Q_s and significantly improved prediction in regions with vegetation compared to the existing τ-based models (Figure 5).

4.4. The Ripple Characteristics and Migration Rate

During the sediment-recirculation experiment, migrating bedforms were observed in both bare and vegetated channels. We classified them as ripples because their height was less than 2 cm (Julien, 2010). The ripple height sampled at one point over time using the Vectrino, $\eta_1 \pm SD(\eta_1)$, agreed with the ripple height identified from the scanned topography, $\eta_2 \pm SD(\eta_2)$, within uncertainty (Table 2). Because the number of ripples sampled by the Vectrino was larger than the number of ripples scanned by the laser sensor (Table 2), further analyses will focus on η_1. For bare channels ($\phi = 0$), the ripple height (η_1) increased between the velocity 0.42 and 0.47 m/s but was constant within measurement uncertainty for a velocity of 0.47 m/s and above (blue triangles in Figure 7a). Previous experimental studies over bare beds have shown that ripple height first increases with increasing U, but at higher velocity, the ripples start to be washed out, and the ripple height decreases with increasing U, and eventually, at sufficiently high velocity, the ripples wash out completely, and the bed load transport enters the plane bed regime (Damgaard et al., 2003; Southard, 1991). For our bare channel cases ($\phi = 0$), ripples were observed for all cases, up to 0.88 m/s, with no decrease

in the ripple height, indicating that the critical velocity for bed forms to be washed out, the transition to plane beds, was larger than $U = 0.88$ m/s. Previous studies (e.g., Poos, 2011; Southard, 1991) suggest that the transition to an upper-regime plane bed occurs when Froude number ($F = U/\sqrt{gh}$) reaches 1, which would put the transition velocity in this study around 1.2 m/s. Our data gave some suggestion that the presence of model vegetation had impacted the ripple height and the transition to plane bed conditions. First, at $U \approx 0.4$ m/s, the case with vegetation ($\phi = 0.005$, the cyan triangle) had larger η_1 than the bare channel case (the dark blue triangle), and at $U \approx 0.3$ m/s, the case with $\phi = 0.012$ (the green triangle) had larger η_1 than the two cases with $\phi = 0.005$ (the cyan triangles), suggesting that at the same pore velocity, model vegetation may have increased ripple height. However, the ripple height decreased for cases with denser vegetation ($\phi = 0.025$, the yellow triangles), for which the ripple height was just 2 mm, barely four times the grain size, indicating that for this stem density, the ripples were nearly washed out at $U \leq 0.2$ m/s. This observation suggested that dense vegetation may reduce the critical velocity at which upper-regime plane bed was formed. This observation that the model vegetation suppressed the formation of ripples was consistent with the observation that the addition of vegetation eliminated bedforms previously observed on a point bar in a manmade stream (Nepf, 2012b; Rominger et al., 2010).

The ripple wavelengths of all bare-bed cases agreed within uncertainty (Table 2 and Figure 7b), consistent with previous studies which indicated that the equilibrium ripple wavelength is only a function of grain size (Baas, 1993). Soulsby et al. (2012) proposed the following empirical relationship:

$$\lambda = d_s(500 + 1881 D_*^{-1.5}), \tag{11}$$

for $1.2 < D_* = [g(\rho_s/\rho - 1)/\nu^2]^{1/3} d_s < 16$. In this study, $D_* = 12.6$, predicting $\lambda = 0.27$ m, which was consistent with average wavelength across all bare channel measurements ($\lambda = 0.27 \pm 0.06$ m). For cases with vegetation, λ decreased with increasing vegetation solid volume fraction (Figure 7b). The data suggested that the ripple wavelength may scale with the mean distance between neighboring dowels aligned in the streamwise direction. Specifically, for $\phi = 0.005$ and 0.012, the streamwise dowel spacing was 0.15 and 0.10 m, respectively, shown with blue and cyan dashed lines in Figure 7b. Except for two cases with large uncertainty (σ_λ), the ripple wavelength was equal to the streamwise stem spacing. Recall that the wavelength could not be measured for the highest solid volume fraction, for which the ripples were nearly washed out. We hypothesize that ripple wavelength scales with vegetation spacing because the physical obstruction provided by the vegetation breaks the hydrodynamic feedback between ripples and flow structure, so that only bed features smaller than the stem spacing can exist. The inhibition of larger scales of hydrodynamic structure by vegetation is similar to the observation that the vegetation breaks apart eddies of a scale much greater than the stem spacing, leaving only eddies of a size similar to vegetation diameter or spacing (Nepf, 1999).

The ripple migration speed, calculated as $U_{\text{ripple}} = \lambda/T$, varied by almost three orders of magnitude (Figure 7c). U_{ripple} increased with increasing U, consistent with previous observations (e.g., Chang, 1939; Sternberg, 1967). For bare channel cases, the variation in U_{ripple} versus U agreed within uncertainty with the empirical relationship suggested by Chang (1939) for $d_s = 0.40$ mm, which is

$$U_{\text{ripple}}/U^5 = (4.5 \pm 0.6) \times 10^2 (\text{m/s})^{-4}, \tag{12}$$

as indicated by the dashed red lines and black lines in Figure 7c. Compared with bare channel cases, U_{ripple} was greater with model vegetation (Table 2). Specifically, at $U \approx 0.4$ m/s, U_{ripple} increased between the bare bed ($\phi = 0$) and $\phi = 0.005$, and at $U \approx 0.3$ m/s, U_{ripple} increased between $\phi = 0.005$ and 0.012 (Figure 7c). The increase in ripple migration speed with increasing ϕ was consistent with the idea that the vegetation-generated turbulence increased bed load transport rate, causing the ripples to migrate faster. However, in most cases, the ripple migration speed with vegetation still agreed within uncertainty with the empirical relation from Chang (1939) developed for bare bed.

In bare channels with ripples, the total bed load transport can be described by the sediment transport associated with migrating ripples (e.g., Crickmore, 1970; Damgaard et al., 2003), that is,

$$Q_s = Q_{s_{\text{ripple}}} = \beta(\eta U_{\text{ripple}}) C_0 \rho_s. \tag{13}$$

Here $C_0 = 0.6$ is a porosity factor, and the coefficient β is the product of the ripple shape factor and the flow separation factor. The ripple shape factor is the fraction of a rectangle with length and height equal to the

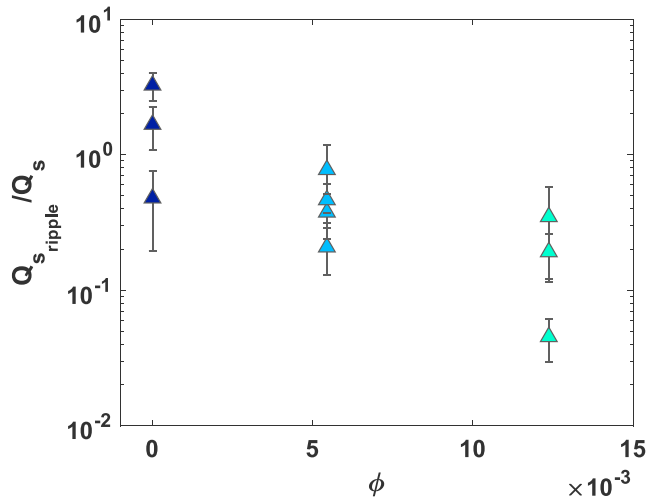

Figure 8. The ripple migration rate $Q_{s_{\text{ripple}}}$ divided by the measured bed load transport rate Q_s as a function of vegetation solid volume fraction ϕ. The vertical error bars were contributed by the uncertainties in η_1, λ, and T (Table 2).

ripple length and height, occupied by the ripple (Kuhnle et al., 2006). $\beta = 0.2$ to 0.8 was suggested in previous studies and should be a constant for the same experimental setup (Damgaard et al., 2003; Kuhnle et al., 2006). For the bare channel measurements in this study, $\beta = 0.43$ provided the minimum *RMSD* between measured bed load transport rate and the bed load transport rate predicted from equation (13), so we will use this value in further analyses for both bare and vegetated channels. The impact of model vegetation on ripple migration rate is considered in Figure 7d, which shows that ripple migration rate varied by almost three orders of magnitude, predominantly due to changes in the magnitude of U_{ripple} (Table 2). Specifically, U_{ripple} increased with increasing ϕ, and this explained the increase in $Q_{s_{\text{ripple}}*}$ with increasing vegetation solid volume fraction.

To examine whether ripple migration was a good estimator of total bed load transport rate in vegetated channels, we considered the ratio of bed load transport estimated from ripple migration rate using equation (13) ($Q_{s_{\text{ripple}}}$) to the measured bed load transport rate Q_s (Figure 8). As expected for the fitted value of β, the average of $Q_{s_{\text{ripple}}}/Q_s$ for bare channels was one. However, as the vegetation solid volume fraction ϕ increased, $Q_{s_{\text{ripple}}}/Q_s$ decreased, indicating that as vegetation volume fraction increased, an increasing fraction of the bed load transport was not associated with ripple migration, which suggested a transition to sheet flow, in which sediment is transported over a plane bed without the formation of bedforms. This was supported by the fact that for cases with $\phi = 0.025$, the measured ripple height was significantly smaller than the other vegetated cases and nearly comparable to the grain size, suggesting an approach to sheet flow in the most densely vegetated channel at a velocity much smaller than the critical velocity for bare channels ($U_{\text{transit}} > 0.88$ m/s as shown in Figure 7a). Similarly, the addition of vegetation to a point bar in a sand river eliminated the previously observed migrating dunes (Figure 8 in Nepf (2012b)). In addition, Przyborowski et al. (2018) observed that the height of migrating bedforms in regions of a channel with vegetation was significantly smaller than in unvegetated regions. Together, these observations suggest that vegetation may reduce the role of migrating bedforms in sediment transport.

5. Summary

A model for predicting the near-bed turbulent kinetic energy (k_t) in vegetated channels with mobile sediment beds was validated using velocity measurements. This k_t model (equation (1)) was combined with the k_t-based bed load transport model proposed by Yang and Nepf (2018) to predict bed load transport rate (Q_s) in vegetated channels based on pore velocity and vegetation volume fraction. The dependence of Q_s on k_t was explained using statistics of individual grain motion recorded by a camera, which showed that Q_s was predominantly controlled by the volume of grains in motion per bed area, which correlated more closely with $\sqrt{k_t}$ than U. For the smaller vegetation solid volume fractions ($\phi = 0.005, 0.012$), the ripple wavelength was set by the stem spacing. For these cases, the presence of model vegetation increased the rate of ripple migration. However, at the higher vegetation solid volume fraction ($\phi = 0.025$), the ripple height was comparable to the grain size, indicating a transition to sheet flow at $U \leq 0.2$ m/s, which was much lower than the transition velocity over bare beds. Finally, the fraction of the total bed load transport carried by the migrating ripples decreased with increasing ϕ, and at the largest vegetation volume fraction ($\phi = 0.025$), the ripples made a negligible contribution to bed load transport, suggesting that vegetation facilitated the transition from bedforms to plane beds with sheet flow.

Acknowledgments
The work was supported by NSF grant EAR 1414499. Judy Q. Yang was supported by the Fellowship for Sustainability funded by the Martin Foundation. The data in this study are tabulated in Judy Qingjun Yang's thesis, which will be available on MIT D-Space (https://dspace.mit.edu/). The authors thank Milani Chatterji-Len and Yinghao Zhang for their assistance with the experiments and John Trowbridge for his insightful comments.

References

Ancey, C., Bohorquez, P., & Heyman, J. (2015). Stochastic interpretation of the advection-diffusion equation and its relevance to bed load transport. *Journal of Geophysical Research: Earth Surface*, *120*, 2529–2551. https//doi.org/10.1002/2014JF003421

Ancey, C., Davison, A., Böhm, T., Jodeau, M., & Frey, P. (2008). Entrainment and motion of coarse particles in a shallow water stream down a steep slope. *Journal of Fluid Mechanics*, *595*, 83–114.

Aubry, N., Holmes, P., Lumley, J. L., & Stone, E. (1988). The dynamics of coherent structures in the wall region of a turbulent boundary layer. *Journal of Fluid Mechanics*, *192*, 115–173.

Baas, J. H. (1993). Dimensional analysis of current ripples in recent and ancient depositional environments (Dissertation), Faculteit Aardwetenschappen.

Bagnold, R. A. (2012). *The physics of blown sand and desert dunes*. Mineola, New York: Courier Corporation.

Batchelor, G. (1951). Pressure fluctuations in isotropic turbulence, *Mathematical Proceedings of the Cambridge Philosophical Society* (Vol. 47, pp. 359–374). Cambridge: Cambridge University Press.

Bennett, S., & Best, J. (1995). Mean flow and turbulence structure over fixed, two-dimensional dunes: Implications for sediment transport and bedform stability. *Sedimentology*, *42*(3), 491–513.

Best, J. (2005). The fluid dynamics of river dunes: A review and some future research directions. *Journal of Geophysical Research*, *110*, F04S02. https://doi.org/10.1029/2004JF000218

Blum, M. D., & Roberts, H. H. (2009). Drowning of the Mississippi delta due to insufficient sediment supply and global sea-level rise. *Nature Geoscience*, *2*(7), 488–491.

Brown, C. B. (1950). Sediment transportation. *Engineering Hydraulics*, *12*, 769–857.

Chang, Y. (1939). Laboratory investigation of flume traction and transportation. *Transactions of the American Society of Civil Engineers*, *104*(1), 1246–1284.

Costanza, R., d'Arge, R., De Groot, R., Farber, S., Grasso, M., Hannon, B., et al. (1997). The value of the world's ecosystem services and natural capital. *Nature*, *387*(6630), 253–260.

Crickmore, M. J. (1970). Effect of flume width on bed-form characteristics. *Journal of the Hydraulics Division*, *96*, 473–496.

Crocker, J. C., & Grier, D. G. (1996). Methods of digital video microscopy for colloidal studies. *Journal of Colloid and Interface Science*, *179*(1), 298–310.

Damgaard, J., Soulsby, R., Peet, A., & Wright, S. (2003). Sand transport on steeply sloping plane and rippled beds. *Journal of Hydraulic Engineering*, *129*(9), 706–719.

Dhont, B., & Ancey, C. (2018). Are bedload transport pulses in gravel bed rivers created by bar migration or sediment waves? *Geophysical Research Letters*, *45*, 5501–5508. https://doi.org/10.1029/2018GL077792

Diplas, P., Dancey, C. L., Celik, A. O., Valyrakis, M., Greer, K., & Akar, T. (2008). The role of impulse on the initiation of particle movement under turbulent flow conditions. *Science*, *322*(5902), 717–720.

Dittrich, A. (1998). *Wechselwirkung Morphologie/Strömung naturnaher Fließgewässer*. Inst. f. Wasserwirtschaft u. Kulturtechnik. Chichester, UK: Wiley.

Einstein, H. A. (1950). *The bed-load function for sediment transportation in open channel flows*. Washington, DC: 1026, US Department of Agriculture.

Etminan, V., Ghisalberti, M., & Lowe, R. J. (2018). Predicting bed shear stresses in vegetated channels. *Water Resources Research*, *54*, 9187–9206. https://doi.org/10.1029/2018WR022811

Etminan, V., Lowe, R. J., & Ghisalberti, M. (2017). A new model for predicting the drag exerted by vegetation canopies. *Water Resources Research*, *53*, 3179–3196. https://doi.org/10.1002/2016WR020090

Fagherazzi, S., Mariotti, G., Wiberg, P. L., & McGLATHERY, K. J. (2013). Marsh collapse does not require sea level rise. *Oceanography*, *26*(3), 70–77.

Furbish, D. J., Haff, P. K., Roseberry, J. C., & Schmeeckle, M. W. (2012). A probabilistic description of the bed load sediment flux: 1. Theory. *Journal of Geophysical Research*, *117*, F03031. https://doi.org/10.1029/2012JF002352

Heathershaw, A., & Thorne, P. (1985). Sea-bed noises reveal role of turbulent bursting phenomenon in sediment transport by tidal currents. *Nature*, *316*(6026), 339–342.

Hofland, B., & Battjes, J. A. (2006). Probability density function of instantaneous drag forces and shear stresses on a bed. *Journal of Hydraulic Engineering*, *132*(11), 1169–1175.

Houssais, M., Ortiz, C. P., Durian, D. J., & Jerolmack, D. J. (2015). Onset of sediment transport is a continuous transition driven by fluid shear and granular creep. *Nature Communications*, *6*, 6527.

Jenkins, W. A., Murray, B. C., Kramer, R. A., & Faulkner, S. P. (2010). Valuing ecosystem services from wetlands restoration in the Mississippi alluvial valley. *Ecological Economics*, *69*(5), 1051–1061.

Jordanova, A. A., & James, C. (2003). Experimental study of bed load transport through emergent vegetation. *Journal of Hydraulic Engineering*, *129*(6), 474–478.

Julien, P. Y. (2010). *Erosion and sedimentation*. Cambridge, UK: Cambridge University Press.

King, A., Tinoco, R., & Cowen, E. (2012). A k–ϵ turbulence model based on the scales of vertical shear and stem wakes valid for emergent and submerged vegetated flows. *Journal of Fluid Mechanics*, *701*, 1–39.

Kothyari, U. C., Hashimoto, H., & Hayashi, K. (2009). Effect of tall vegetation on sediment transport by channel flows. *Journal of Hydraulic Research*, *47*(6), 700–710.

Kuhnle, R., Horton, J., Bennett, S., & Best, J. (2006). Bed forms in bimodal sand–gravel sediments: Laboratory and field analysis. *Sedimentology*, *53*(3), 631–654.

Kwoll, E., Venditti, J., Bradley, R., & Winter, C. (2016). Flow structure and resistance over subaquaeous high-and low-angle dunes. *Journal of Geophysical Research: Earth Surface*, *121*, 545–564. https://doi.org/10.1002/2015JF003637

Lajeunesse, E., Malverti, L., & Charru, F. (2010). Bed load transport in turbulent flow at the grain scale: Experiments and modeling. *Journal of Geophysical Research*, *115*, F04001. https://doi.org/10.1029/2009JF001628

Ma, H., Nittrouer, J. A., Naito, K., Fu, X., Zhang, Y., Moodie, A. J., et al. (2017). The exceptional sediment load of fine-grained dispersal systems: Example of the Yellow River, China. *Science Advances*, *3*(5), e1603114.

Manners, R. B., Wilcox, A. C., Kui, L., Lightbody, A. F., Stella, J. C., & Sklar, L. S. (2015). When do plants modify fluvial processes? Plant-hydraulic interactions under variable flow and sediment supply rates. *Journal of Geophysical Research: Earth Surface*, *120*, 325–345. https://doi.org/10.1002/2014JF003265

Mazumder, R. (2000). Turbulence–particle interactions and their implications for sediment transport and bedform mechanics under unidirectional current: Some recent developments. *Earth-Science Reviews*, *50*(1-2), 113–124.

McLeod, E., Chmura, G. L., Bouillon, S., Salm, R., Björk, M., Duarte, C. M., et al. (2011). A blueprint for blue carbon: Toward an improved understanding of the role of vegetated coastal habitats in sequestering CO_2. *Frontiers in Ecology and the Environment*, *9*(10), 552–560.

Narayan, S., Beck, M. W., Wilson, P., Thomas, C. J., Guerrero, A., Shepard, C. C., et al. (2017). The value of coastal wetlands for flood damage reduction in the northeastern USA. *Scientific Reports*, *7*(1), 9463.

Nelson, J. M., Shreve, R. L., McLean, S. R., & Drake, T. G. (1995). Role of near-bed turbulence structure in bed load transport and bed form mechanics. *Water Resources Research*, *31*(8), 2071–2086.

Nepf, H. (1999). Drag, turbulence, and diffusion in flow through emergent vegetation. *Water Resources Research*, *35*(2), 479–489.
Nepf, H. M. (2012a). Flow and transport in regions with aquatic vegetation. *Annual Review of Fluid Mechanics*, *44*, 123–142.
Nepf, H. M. (2012b). Hydrodynamics of vegetated channels. *Journal of Hydraulic Research*, *50*(3), 262–279.
Nino, Y., & Garcia, M. (1996). Experiments on particle–turbulence interactions in the near–wall region of an open channel flow: Implications for sediment transport. *Journal of Fluid Mechanics*, *326*, 285–319.
Poos, W. (2011). Stability diagram of upper flow regime bedforms. An experimental study (Master's thesis). Utrecht University.
Przyborowski, Ł., Łoboda, A., & Bialik, R. (2018). Experimental investigations of interactions between sand wave movements, flow structure, and individual aquatic plants in natural rivers: A case study of Potamogeton pectinatus L. *Water*, *10*(9), 1166.
Radice, A., & Ballio, F. (2008). Double-average characteristics of sediment motion in one-dimensional bed load. *Acta Geophysica*, *56*(3), 654–668.
Radice, A., Ballio, F., & Nikora, V. (2009). On statistical properties of bed load sediment concentration. *Water resources research*, *45*, W06501. https://doi.org/10.1029/2008WR007192
Rominger, J. T., Lightbody, A. F., & Nepf, H. M. (2010). Effects of added vegetation on sand bar stability and stream hydrodynamics. *Journal of Hydraulic Engineering*, *136*(12), 994–1002.
Roseberry, J. C., Schmeeckle, M. W., & Furbish, D. J. (2012). A probabilistic description of the bed load sediment flux: 2. Particle activity and motions. *Journal of Geophysical Research*, *117*, F03032. https://doi.org/10.1029/2012JF002353
Rubey, W. W. (1933). Settling velocity of gravel, sand, and silt particles. *American Journal of Science*, *25*(148), 325–338.
Salim, S., Pattiaratchi, C., Tinoco, R., Coco, G., Hetzel, Y., Wijeratne, S., & Jayaratne, R. (2017). The influence of turbulent bursting on sediment resuspension under unidirectional currents. *Earth Surface Dynamics*, *5*(3), 399–425.
Schmeeckle, M. W. (2014). The role of velocity, pressure, and bed stress fluctuations in bed load transport over bed forms: Numerical simulation downstream of a backward-facing step. *Earth Surface Dynamics Discussions*, *2*(2), 715–732.
Shih, W., Diplas, P., Celik, A. O., & Dancey, C. (2017). Accounting for the role of turbulent flow on particle dislodgement via a coupled quadrant analysis of velocity and pressure sequences. *Advances in Water Resources*, *101*, 37–48.
Smart, G., & Habersack, H. (2007). Pressure fluctuations and gravel entrainment in rivers. *Journal of Hydraulic Research*, *45*(5), 661–673.
Soulsby, R., Whitehouse, R., & Marten, K. (2012). Prediction of time-evolving sand ripples in shelf seas. *Continental Shelf Research*, *38*, 47–62.
Southard, J. B. (1991). Experimental determination of bed-form stability. *Annual Review of Earth and Planetary Sciences*, *19*(1), 423–455.
Stapleton, K., & Huntley, D. (1995). Seabed stress determinations using the inertial dissipation method and the turbulent kinetic energy method. *Earth Surface Processes and Landforms*, *20*(9), 807–815.
Sternberg, R. W. (1967). Measurements of sediment movement and ripple migration in a shallow marine environment. *Marine Geology*, *5*(3), 195–205.
Sumer, B. M., Chua, L. H., Cheng, N.-S., & Fredsøe, J. (2003). Influence of turbulence on bed load sediment transport. *Journal of Hydraulic Engineering*, *129*(8), 585–596.
Sumer, B. M., & Oguz, B. (1978). Particle motions near the bottom in turbulent flow in an open channel. *Journal of Fluid Mechanics*, *86*(1), 109–127.
Tanino, Y., & Nepf, H. (2007). Experimental investigation of lateral dispersion in aquatic canopies. *Paper presented at 32nd Congress-International Association for Hydraulic Research* (p.152). Venice, Italy. 1–6 Jul.
Tanino, Y., & Nepf, H. M. (2008). Lateral dispersion in random cylinder arrays at high Reynolds number. *Journal of Fluid Mechanics*, *600*, 339–371.
Tinoco, R. O., & Coco, G. (2016). A laboratory study on sediment resuspension within arrays of rigid cylinders. *Advances in Water Resources*, *92*, 1–9.
Tinoco, R., & Coco, G. (2018). Turbulence as the main driver of resuspension in oscillatory flow through vegetation. *Journal of Geophysical Research: Earth Surface*, *123*, 891–904. https://doi.org/10.1002/2017JF004504
Van Rijn, L. C. (2007). Unified view of sediment transport by currents and waves. I: Initiation of motion, bed roughness, and bed-load transport. *Journal of Hydraulic engineering*, *133*(6), 649–667.
Vollmer, S., & Kleinhans, M. G. (2007). Predicting incipient motion, including the effect of turbulent pressure fluctuations in the bed. *Water Resources Research*, *43*, W05410. https://doi.org/10.1029/2006WR004919
Whiting, P. J., & Dietrich, W. E. (1990). Boundary shear stress and roughness over mobile alluvial beds. *Journal of Hydraulic Engineering*, *116*(12), 1495–1511.
Wong, M., Parker, G., DeVries, P., Brown, T. M., & Burges, S. J. (2007). Experiments on dispersion of tracer stones under lower-regime plane-bed equilibrium bed load transport. *Water Resources Research*, *43*, W03440. https://doi.org/10.1029/2006WR005172
Yager, E., & Schmeeckle, M. (2013). The influence of vegetation on turbulence and bed load transport. *Journal of Geophysical Research: Earth Surface*, *118*, 1585–1601. https://doi.org/10.1002/jgrf.20085
Yang, J., Chung, H., & Nepf, H. (2016). The onset of sediment transport in vegetated channels predicted by turbulent kinetic energy. *Geophysical Research Letters*, *43*, 11,261–11,268. https://doi.org/10.1002/2016GL071092
Yang, J. Q., Kerger, F., & Nepf, H. M. (2015). Estimation of the bed shear stress in vegetated and bare channels with smooth beds. *Water Resources Research*, *51*, 3647–3663. https://doi.org/10.1002/2014WR016042
Yang, J., & Nepf, H. (2018). A turbulence-based bed-load transport model for bare and vegetated channels. *Geophysical Research Letters*, *45*, 10,428–10,436. https://doi.org/10.1029/2018GL079319
Zanke, U. (2003). On the influence of turbulence on the initiation of sediment motion. *International Journal of Sediment Research*, *18*(1), 17–31.
Zedler, J. B., & Kercher, S. (2005). Wetland resources: Status, trends, ecosystem services, and restorability. *Annual Review of Environment and Resources*, *30*, 39–74.
Zhang, Y., Tang, C., & Nepf, H. (2018). Turbulent kinetic energy in submerged model canopies under oscillatory flow. *Water Resources Research*, *54*, 1734–1750. https://doi.org/10.1002/2017WR021732

View publication stats